mathematics

MDPI

Article

# A Numerical Approach for the Heat Transfer Flow of Carboxymethyl Cellulose-Water Based Casson Nanofluid from a Solid Sphere Generated by Mixed Convection under the Influence of Lorentz Force

**Firas A. Alwawi [1,2,*], Hamzeh T. Alkasasbeh [3], Ahmed M. Rashad [4] and Ruwaidiah Idris [1]**

[1] Faculty of Ocean Engineering Technology and Informatics, University Malaysia Terengganu, 21030 Kual Nerus, Terengganu, Malaysia; ruwaidiah@umt.edu.my
[2] Department of Mathematics, College of Sciences and Humanities in Al-Kharj, Prince Sattam bin Abdulaziz University, Al-Kharj 11942, Saudi Arabia
[3] Department of Mathematics, Faculty of Science, Ajloun National University, P.O. Box 43, Ajloun 26810, Jordan; alkasasbehh@gmail.com
[4] Department of Mathematics, Aswan University, Faculty of Science, Aswan 81528, Egypt; am_rashad@yahoo.com
* Correspondence: f.alwawi@psau.edu.sa

Received: 9 June 2020; Accepted: 2 July 2020; Published: 4 July 2020

**Abstract:** The heat transfer of a carboxymethyl cellulose aqueous solution (CMC-water) based Casson nanofluid, flowing under the impact of a variable-strength magnetic field in mixed convection around a solid sphere, has been examined in this work. Aluminum (Al), copper (Cu), and silver (Ag) nanoparticles were employed to support the heat transfer characteristics of the host fluid. A numerical approach called the Keller-box method (KBM) was used to solve the governing system for the present problem, and also to examine and analyze the numerical and graphic results obtained by the MATLAB program, verifying their accuracy through comparing them with the prior literature. The results demonstrate that a Al–CMC-water nanoliquid is superior in terms of heat transfer rate and skin friction. The velocity of CMC-water is higher with Ag compared to Al–CMC-water, and Ag–CMC-water possesses the lowest temperature. Growing mixed parameter values result in a rising skin friction, velocity and Nusselt number or decline in temperature.

**Keywords:** MHD; CMC-water; Casson fluid; mixed convection; solid sphere

## 1. Introduction

Carboxymethyl cellulose (CMC), also known as cellulose gum [1], has many features: a high solubility, clarity of its solutions, the ability to hold water, controlled crystal growth, and it can modify viscosity, in addition to its capacity to fit the required smooth texture or body. These multifunctional aspects of a non-toxic cellulose derivative are why it is utilized in many industries and technical applications. It is employed to enhance moisturizing impact due to its polymeric structure that works as a film-forming factor [2,3]. CMC is utilized in paper industries and pharmaceuticals and is also used to stabilize clay particles [2,4] and others [5–10]. In view of the massive uses of CMC, many researchers have devoted their time to studying it. Saqib et al. [11,12] employed a Caputo–Fabrizio fractional derivative (CFFD) approach and an Atangana–Baleanu fractional derivative (ABFD) approach alongside the Laplace technique to investigate the convection flow of CMC-water nanofluid. They confirmed that multiple wall carbon nanotubes are more effective in terms of improved heat transfer, and that the velocity of CMC-water is higher with

multiple wall carbon nanotubes. Rahmati et al. [13] examined the laminar flow of a CMC-aqueous solution in a horizontal 2D microtube. Their findings revealed that the slip velocity coefficient contributed notably to the growth of the heat transfer rate, and significantly reduced the friction factor of the horizontal microtube wall.

The real reason for using nanotechnology is its capacity to work at the molecular level, atom-by-atom, to make large structures via essentially novel molecular organization. The actual birth of nanotechnology was at the end of 1959 when it was introduced by physicist Richard P Feynman [14]. He concluded that the physical properties of materials change depending on the scale of its molecules, and also posed two challenges: writing "Encyclopedia Britannica" on the head of a pin and making the nanometer. Two decades later, IBM Zurich scientists were able to invent the scanning tunneling microscope, which enabled scientists for the first time to observe materials at the atomic scale, a paradigm shift that had significantly contributed to the spread of nanotechnology in all industrialized countries by the 1990s. In the heat transfer field, Choi and Eastman [15] incorporated nanotechnology unprecedentedly through immersed metallic nanoparticles in a base fluid. These ultrafine particles possessed extraordinary properties that made them notably improve the thermal conductivity of the ordinary fluid. Buongiorno [16] developed a mathematical model that shows that the heat transfer rate is affected by several factors other than the thermal conductivity impact. Tiwari and Das [17] also developed a mathematical model to consider the solid volume fraction. Recently, many researchers have used the Tiwari and Das model to examine the nanofluid flow behavior of nanoparticles. Swalmeh et al. [18] used the Tiwari and Das model to investigate the behavior of micropolar nanofluid from a sphere. Selimefendigil et al. [19] analyzed the magnetohydrodynamic (MHD) combined convection flow of a nanofluid in a lid-driven triangular cavity by the use of the Tiwari and Das model. Alwawi et al. [20] employed the Tiwari and Das model to simulate the flow behavior of a sodium alginate based Casson nanofluid from a sphere. Metal nanoparticles are distinguished by excellent electrical and thermal conductivity, chemical stability, optical and magnetic distinct properties and also, they have a high surface-to-volume ratio. However, in this study aluminum (Al), copper (Cu), and silver (Ag) metal nanoparticles were used because of their similar thermo-physical properties and their common uses and many applications in polymers and pharmaceuticals [21–23], which may be due to their presence accompanied with the presence of CMC-water in these applications.

In real life, mixed convection plays a pivotal role in many engineering and industrial applications. It appears clearly in the cooling of electronic devices and nuclear reactors, food processing, and solar collectors. In addition, Lorentz forces, generated by the passage of a magnetic field via a flowing conducting fluid, has occupied a prominent place in several modern processes of metallurgy and metalworking. Makinde and Aziz [24] analyzed mixed convection on a vertical plate in a porous medium considering the MHD impact and convective boundary condition. Tham et al. [25] studied the boundary layer flow of nanofluid with the MHD effect. Chamkha et al. [26] investigated the magneto-mixed convection flow of ferrofluids in the presence of a partial slip. Here are some of the most important recently conducted studies related to MHD mixed convection [27–32].

Casson's model [33] was developed in 1959 to be able to predict the behavior of non-Newtonian fluids efficiently, and since then it has demonstrated its competence by foretelling the behavior of shear-thinning fluids, such as human blood, honey, concentrated fruit juice, ketchup, and others. Later a considerable number of articles employed this model. Malik et al. [34] employed the Runge–Kutta–Fehlberg technique to examine the flow of a Casson nanoliquid about a vertical cylinder. Mukhopadhyay et al. [35] emphasized that the flow separation could be curbed by raising the Casson parameter. Mustafa et al. [36] investigated the convection of Casson fluid from a stretching sheet taking into account viscous dissipation. See also these recent and efficient studies [37–41].

To the best of our knowledge, and judging by the prior literature, no study has been conducted on the heat transfer of a CMC-based Casson nanoliquid induced by combined convection past a solid sphere with a MHD influence via the KBM that has been investigated in this work. It is also an

extension and development of these studies [20,25,42–44] which may be useful in academic studies, polymer processes, pharmaceutical and food industries, and others.

## 2. Basic Governing Equations

A MHD mixed convection flow of three types of metals (Al, Ag, Cu) in a host Casson fluid over an isothermal sphere of radius $a$ with a prescribed wall 1 temperature $T_w$ and ambient 1 temperature $T_\infty$ were taken into account. Additionally, a heated and cooled sphere ($T_w > T_\infty$ & $T_w < T_\infty$, respectively) was considered.

Figure 1 depicts the schematic configuration and geometrical coordinates, where $U_\infty$, and $g$ are the free stream velocity, and the gravity vector, respectively. The $(\tilde{\xi}, \tilde{\eta})$ coordinates were measured along the circumference of the sphere at the stagnation point ($\tilde{\xi} \approx 0$), and the distance normal to the surface of the sphere, respectively.

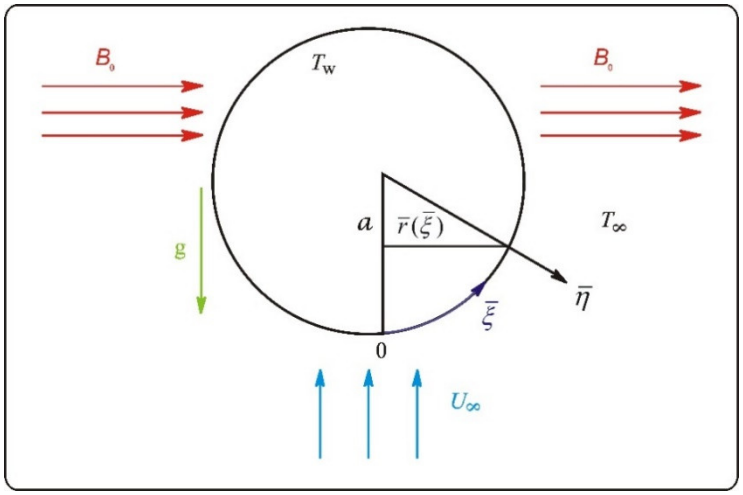


**Figure 1.** Schematic configuration of the problem.

Based on the previous assumption, the governing PDEs. for the Casson nanofluid are:

$$\frac{\partial}{\partial \tilde{\xi}}(r\tilde{u}) + \frac{\partial}{\partial \tilde{\eta}}(r\tilde{v}) = 0, \tag{1}$$

$$\tilde{u}\frac{\partial \tilde{u}}{\partial \tilde{\xi}} + \tilde{v}\frac{\partial \tilde{u}}{\partial \tilde{\eta}} = \tilde{u}_e \frac{d\tilde{u}_e}{d\tilde{\xi}} + \upsilon_{nf}\left(1+\frac{1}{\beta}\right)\frac{\partial^2 \tilde{u}}{\partial \tilde{\eta}^2} + \left(\frac{\chi\rho_s\beta_s + (1-\chi)\rho_f\beta_f}{\rho_{nf}}\right) g(T-T_\infty)\sin\left(\frac{\tilde{\xi}}{a}\right) - \frac{\sigma_{nf}B_0^2}{\rho_{nf}}\tilde{u}, \tag{2}$$

$$\tilde{u}\frac{\partial T}{\partial \tilde{\xi}} + \tilde{v}\frac{\partial T}{\partial \tilde{\eta}} = \alpha_{nf}\frac{\partial^2 T}{\partial \tilde{\eta}^2}, \tag{3}$$

When they are associated with the boundary conditions:

$$\tilde{u} = \tilde{v} = 0,\ T = T_w, \text{ as } \tilde{\eta} = 0, \quad \tilde{u} \to \tilde{u}_e(\tilde{\xi}),\ T \to T_\infty, \text{ as } \tilde{\eta} \to \infty. \tag{4}$$

where $\tilde{r}(\tilde{\xi})$ and $\tilde{u}_e(\tilde{\xi})$ are given by:

$$\tilde{r}(\tilde{\xi}) = a\sin(\tilde{\xi}/a), \text{ and } \tilde{u}_e(\tilde{\xi}) = \frac{3}{2}U_\infty \sin(\tilde{\xi}/a), \tag{5}$$

The properties of the nanofluid (defined by [45]) are:

$$\frac{\sigma_{nf}}{\sigma_f}=1+\frac{3(\sigma-1)\chi}{(\sigma+2)-(\sigma-1)\chi},\ \sigma=\frac{\sigma_s}{\sigma_f},\ \ \frac{k_{nf}}{k_f}=\frac{\left(k_s+2k_f\right)-2\chi\left(k_f-k_s\right)}{\left(k_s+2k_f\right)+\chi\left(k_f-k_s\right)},\ \ \mu_{nf}=\frac{\mu_f}{(1-\chi)^{2.5}},$$
$$\left(\rho c_p\right)_{nf}=(1-\chi)\left(\rho c_p\right)_f+\chi\left(\rho c_p\right)_s,\ \rho_{nf}=(1-\chi)\rho_f+\chi\rho_s,\ \alpha_{nf}=\frac{k_{nf}}{\left(\rho c_p\right)_{nf}}, \tag{6}$$

The following non-dimensional variables that are expressed by Rashad et al. [46] were used:

$$x=\frac{\tilde{\xi}}{a},\ y=\mathrm{Re}^{1/2}\left(\frac{\tilde{\eta}}{a}\right),\ r(\tilde{\xi})=\frac{\tilde{r}(\tilde{\xi})}{a},\ u=\frac{\tilde{u}}{U_\infty},$$

$$v=\mathrm{Re}^{1/2}\left(\frac{\tilde{v}}{U_\infty}\right),\ u_e(\xi)=\frac{\overline{u}_e(\tilde{\xi})}{U_\infty},\ \theta=\frac{T-T_\infty}{T_w-T_\infty}, \tag{7}$$

where $\mathrm{Re}=U_\infty\frac{a}{v_f}$ is the Reynolds number.

By substituting Equation (7) into Equations (1)–(4) we get the following non-dimensional equations:

$$\frac{\partial}{\partial\xi}(ru)+\frac{\partial}{\partial\eta}(rv)=0, \tag{8}$$

$$u\frac{\partial u}{\partial\xi}+v\frac{\partial u}{\partial\eta}=u_e(\xi)\frac{du_e}{d\xi}+\frac{\rho_f}{\rho_{nf}}\frac{1}{(1-\chi)^{2.5}}\left(1+\frac{1}{\beta}\right)\frac{\partial^2u}{\partial\eta^2}+\left(\frac{\chi\rho_s\beta_s+(1-\chi)\rho_f\beta_f}{\rho_{nf}}\right)\lambda\theta\sin\xi-\frac{\rho_f\sigma_{nf}}{\rho_{nf}\sigma_f}Mu, \tag{9}$$

$$u\frac{\partial\theta}{\partial\xi}+v\frac{\partial\theta}{\partial\eta}=\frac{1}{\mathrm{Pr}}\left(\frac{k_{nf}/k_f}{(1-\chi)+\chi\left(\rho c_p\right)_s/\left(\rho c_p\right)_f}\right)\frac{\partial^2\theta}{\partial\eta^2}, \tag{10}$$

here $M=\left(\frac{\sigma_f\beta_0^2a}{\rho_fv_f}\right)$, $\mathrm{Pr}=\frac{v_f}{\alpha_f}$, $\lambda=Gr/\mathrm{Re}^2$, and $Gr=g\beta_f(T_w-T_\infty)\frac{a^3}{v_f^2}$.

and the dimensionless boundary conditions are:

$$u=v=0,\ \theta=1,\ \text{at}\ \eta=0,$$

$$u\to\frac{3}{2}\sin\tilde{\xi},\ \theta\to0,\ \text{as}\ \eta\to\infty. \tag{11}$$

To solve the non-dimensional Equations (8)–(10), associated with the boundary conditions in Equation(11), defined the non-dimensional stream function $\psi$ is defined as the following (defined by Nazar et al. [43]):

$$\psi=\tilde{\xi}r(\tilde{\xi})F(\tilde{\xi},\tilde{\eta}),\ \theta=\theta(\tilde{\xi},\tilde{\eta}),$$

$$u=\frac{1}{r}\frac{\partial\psi}{\partial\tilde{\eta}}\ \text{and}\ v=-\frac{1}{r}\frac{\partial\psi}{\partial\tilde{\xi}} \tag{12}$$

By using Equation (12), the non-dimensional Equations (8)–(10) are reduced to:

$$\frac{\rho_f}{\rho_{nf}}\frac{1}{(1-\chi)^{2.5}}\left(1+\frac{1}{\beta}\right)\frac{\partial^3 F}{\partial\eta^3}+(1+\xi\cot\xi)F\frac{\partial^2 F}{\partial\eta^2}-\left(\frac{\partial F}{\partial\eta}\right)^2-\frac{\rho_f\sigma_{nf}}{\rho_{nf}\sigma_f}M\frac{\partial F}{\partial\eta}$$
$$+\left(\frac{\chi\rho_s\beta_s/\beta_f+(1-\chi)\rho_f}{\rho_{nf}}\right)\lambda\theta\frac{\sin\xi}{\xi}+\frac{9}{4}\frac{\sin\xi\cos\xi}{\xi}=\xi\left(\frac{\partial F}{\partial\eta}\frac{\partial^2 F}{\partial\xi\partial\eta}-\frac{\partial F}{\partial\xi}\right. \quad (13)$$

$$\frac{1}{\Pr}\left(\frac{k_{nf}/k_f}{(1-\chi)+\chi\left(\rho c_p\right)_s/\left(\rho c_p\right)_f}\right)\frac{\partial^2\theta}{\partial\eta^2}+(1+\xi\cot\xi)F\frac{\partial\theta}{\partial\eta}=\xi\left(\frac{\partial F}{\partial\eta}\frac{\partial\theta}{\partial\xi}-\frac{\partial F}{\partial\xi}\frac{\partial\theta}{\partial\eta}\right), \quad (14)$$

and the boundary conditions become:

$$\frac{\partial F}{\partial\eta}=F=0,\ \theta=1 \quad \text{at} \quad \eta=0,$$

$$\frac{\partial F}{\partial\eta}\to\frac{3}{2}\frac{\sin\xi}{\xi},\ \theta\to 0, \quad \text{as} \quad \eta\to\infty. \quad (15)$$

At the stagnation point of the sphere when ( $\overline{\xi}\approx 0$ ), Equations (13)–(15) reduce to:

$$\frac{\rho_f}{\rho_{nf}}\frac{1}{(1-\chi)^{2.5}}\left(1+\frac{1}{\beta}\right)F'''+2FF''-(F')^2-\frac{\rho_f\sigma_{nf}}{\rho_{nf}\sigma_f}MF'$$
$$+\left(\frac{\chi\rho_s\beta_s/\beta_f+(1-\chi)\rho_f}{\rho_{nf}}\right)\lambda\theta+\frac{9}{4}=0, \quad (16)$$

$$\frac{1}{\Pr}\left(\frac{k_{nf}/k_f}{(1-\chi)+\chi\left(\rho c_p\right)_s/\left(\rho c_p\right)_f}\right)\theta''+2F\theta'=0, \quad (17)$$

The subject to

$$F'=F=0,\ \theta=1 \quad \text{at} \quad \eta=0,$$

$$F'\to\frac{3}{2},\ \theta\to 0, \quad \text{as} \quad \eta\to\infty. \quad (18)$$

In this work two physical quantities were taken into consideration, specifically the local skin friction coefficient $C_f$ and the local Nusselt number $Nu$, which are given by Molla et al. [47]:

$$C_f=\left(\frac{\tau_w}{\rho U_\infty^2}\right), \quad Nu=\left(\frac{aq_w}{k_f(T_w-T_\infty)}\right), \quad (19)$$

where

$$\tau_w=\mu_{nf}\left(\frac{\partial\tilde{u}}{\partial\tilde{\eta}}\right)_{\tilde{\eta}=0}, \quad q_w=-k_{nf}\left(\frac{\partial T}{\partial\tilde{\eta}}\right)_{\tilde{\eta}=0}. \quad (20)$$

Using Equation(7) and Equation(11), $C_f$ and $Nu$ are turned into:

$$\mathrm{Re}^{1/2}C_f=\frac{1}{(1-\chi)^{2.5}}\left(1+\frac{1}{\beta}\right)\xi\frac{\partial^2 F}{\partial\eta^2}(\xi,0), \quad \mathrm{Re}^{-1/2}Nu=\frac{-k_{nf}}{k_f}\left(\frac{\partial\theta}{\partial\eta}\right)_{\eta=0}. \quad (21)$$

## 3. Numerical Approach

In 1970 Keller [48] was first proposed the Keller-box method. About a decade later, this method became more popular when Jones [49] found a solution for boundary layer problems. Cebeci and Bradshaw [50] provided a detailed explanation of the Keller-box procedure, which we employed it in the current paper to construct the solution for the problem.

### *3.1. The Finite-Difference Method*

In order to transform Equations (13) and (14) to first order equations, new independent unknowns will be defined as follows:

$w(\xi,\eta), z(\xi,\eta), p(\xi,\eta),$ and $g(\xi,\eta),$ where the temperature variable $\theta(\xi,\eta)$ is replaced by $g(\xi,\eta)$, and

$$\begin{aligned} F' &= w, \\ w' &= z, \\ g' &= p, \end{aligned} \tag{22}$$

Thus, the Equations (13)–(15) are converted to:

$$\frac{\rho_f}{\rho_{nf}}\frac{1}{(1-\chi)^{2.5}}\left(1+\frac{1}{\beta}\right)z' + (1+\xi\cot\xi)Fz - w^2 - \frac{\rho_f\sigma_{nf}}{\rho_{nf}\sigma_f}Mw + \left(\frac{\chi\rho_s\beta_s/\beta_f + (1-\chi)\rho_f}{\rho_{nf}}\right)\lambda g\frac{\sin\xi}{\xi} + \frac{9}{4}\frac{\sin\xi\cos\xi}{\xi} = \xi\left(w\frac{\partial w}{\partial\xi} - z\frac{\partial F}{\partial\xi}\right), \tag{23}$$

$$\frac{1}{\mathrm{Pr}}\left(\frac{k_{nf}/k_f}{(1-\chi)+\chi(\rho c_p)_s/(\rho c_p)_f}\right)p' + (1+\xi\cot\xi)Fp = \xi\left(w\frac{\partial g}{\partial\xi} - p\frac{\partial F}{\partial\xi}\right), \tag{24}$$

Subject to:

$$w(\xi,0) = F(\xi,0) = 0,\ g(\xi,0) = 1,$$

$$w(\xi,\infty) = \frac{3}{2}\frac{\sin\xi}{\xi}, g(\xi,\infty) = 0, \tag{25}$$

where the prime notation denotes the 1st derivative with respect to $\eta$,

Next the finite-difference form of Equation (22) for the midpoint $(\xi^n, \eta_{j-1/2})$ of the segment, and find the finite difference form of Equations (23) and (24) about the midpoint $(\xi^{n-1/2}, \eta_{j-1/2})$ of the rectangle have been obtained as:

$$F_j^n - F_{j-1}^n - \frac{h_j}{2}\left(w_j^n + w_{j-1}^n\right) = 0. \tag{26}$$

$$w_j^n - w_{j-1}^n - \frac{h_j}{2}\left(z_j^n + z_{j-1}^n\right) = 0. \tag{27}$$

$$g_j^n - g_{j-1}^n - \frac{h_j}{2}\left(p_j^n + p_{j-1}^n\right) = 0. \tag{28}$$

$$\begin{aligned}&\frac{\rho_f}{\rho_{nf}}\frac{1}{(1-\chi)^{2.5}}\left(1+\frac{1}{\beta}\right)\left(z_j^n-z_{j-1}^n\right)+\left(\frac{A+\alpha}{4}\right)h_j(F_j^n+F_{j-1}^n)(z_j^n+z_{j-1}^n)-\left(\frac{1+\alpha}{4}\right)h_j(w_j^n+w_{j-1}^n)^2\\&+\left(\frac{\alpha}{2}\right)h_j z_{j-1/2}^{n-1}(F_j^n+F_{j-1}^n)+\frac{1}{2}\left(\frac{\chi\rho_s\left(\beta_s/\beta_f\right)+(1-\chi)\rho_f}{\rho_{nf}}\right)\frac{\sin x^{n-1/2}}{x^{n-1/2}}\lambda h_j(g_j^n+g_{j-1}^n)\\&-\frac{1}{2}\frac{\rho_f\delta_{nf}}{\rho_{nf}\delta_f}Mh_j(w_j^n+w_{j-1}^n)-\left(\frac{\alpha}{2}\right)h_jF_{j-1/2}^{n-1}(z_j^n+z_{j-1}^n)+\frac{9}{4}\frac{\sin x^{n-1/2}\cos x^{n-1/2}}{x^{n-1/2}}h_j=\left(R_1\right)_{j-1/2}^{n-1}\end{aligned}\tag{29}$$

$$\begin{aligned}&\frac{1}{\mathrm{Pr}}\frac{k_{nf}/k_f}{\left((1-\chi)(\rho C_p)_f+\chi\left(\rho c_p\right)_s/\left(\rho c_p\right)_f\right)}\left(p_j^n-p_{j-1}^n\right)-\frac{\alpha}{4}h_j(w_j^n+w_{j-1}^n)(g_j^n+g_{j-1}^n)\\&+\frac{A+\alpha}{4}h_j(F_j^n+F_{j-1}^n)(p_j^n+p_{j-1}^n)+\frac{\alpha}{2}h_j(w_j^n+w_{j-1}^n)g_{j-1/2}^{n-1}-\frac{\alpha}{2}h_jw_{j-1/2}^{n-1}(g_j^n+g_{j-1}^n)\\&-\frac{\alpha}{2}h_j(p_j^n-p_{j-1}^n)F_{j-1/2}^{n-1}+\frac{\alpha}{2}h_jp_{j-1/2}^{n-1}(F_j^n+F_{j-1}^n)=\left(R_2\right)_{j-1/2}^{n-1}\end{aligned}\tag{30}$$

where

$$\alpha=\frac{x^{n-1/2}}{k_n},A=\left(1+x^{n-1/2}\cot x^{n-1/2}\right),\quad k_n is\ \Delta\xi,\ \text{and}\ \ h_j\ is\Delta\eta$$

$$\left(R_1\right)_{j-1/2}^{n-1}=-h_j\left(\begin{array}{l}\dfrac{\rho_f}{\rho_{nf}}\dfrac{1}{(1-\chi)^{2.5}}\left(1+\dfrac{1}{\beta}\right)\dfrac{\left(z_j^n-z_{j-1}^n\right)}{h_j}+(A-\alpha)F_{j-1/2}^nz_{j-1/2}^n\\+(\alpha-1)\left(w_{j-1/2}^n\right)^2-\dfrac{\rho_f\sigma_{nf}}{\rho_{nf}\sigma_f}Mw_{j-1/2}^n+\dfrac{9}{4}\dfrac{\sin x^{n-1/2}\cos x^{n-1/2}}{x^{n-1/2}}\\+\left(\dfrac{\chi\rho_s\left(\beta_s/\beta_f\right)+(1-\chi)\rho_f}{\rho_{nf}}\right)\dfrac{\sin x^{n-1/2}}{x^{n-1/2}}\lambda g_{j-1/2}^n\end{array}\right)^{n-1}$$

$$\left(R_2\right)_{j-1/2}^{n-1}=-h_j\left(\begin{array}{l}\dfrac{1}{\mathrm{Pr}}\dfrac{k_{nf}/k_f}{\left((1-\chi)(\rho C_p)_f+\chi\left(\rho c_p\right)_s/\left(\rho c_p\right)_f\right)}\dfrac{\left(p_j^n-p_{j-1}^n\right)}{h_j}\\+\left(A-\alpha\right)F_{j-1/2}^np_{j-1/2}^n+\alpha w_{j-1/2}^ng_{j-1/2}^n\end{array}\right)^{n-1}\tag{31}$$

when $\xi=\xi^n$ the boundary conditions become:

$$F_0^n=w_0^n=0,\ g_0^n=1,$$

$$w_J^n=\frac{3}{2}\frac{\sin\xi}{\xi},\ g_J^n=0,\tag{32}$$

### *3.2. Newton's Method*

Applying Newton's method on the system shown in Equations (26)–(30) to obtains:

$$\delta F_j-\delta F_{j-1}-\frac{1}{2}h_j\left(\delta w_j+\delta w_{j-1}\right)=\left(r_1\right)_{j-1/2}\tag{33}$$

$$\delta w_j-\delta w_{j-1}-\frac{1}{2}h_j\left(\delta z_j+\delta z_{j-1}\right)=\left(r_2\right)_{j-1/2}\tag{34}$$

$$\delta g_j - \delta g_{j-1} - \frac{1}{2} h_j \left( \delta p_j + \delta p_{j-1} \right) = \left( r_3 \right)_{j-1/2} \tag{35}$$

$$\begin{aligned} \left( a_1 \right)_j \delta z_j + \left( a_2 \right)_j \delta z_{j-1} + \left( a_3 \right)_j \delta F_j + \left( a_4 \right)_j \delta F_{j-1} + \left( a_5 \right)_j \delta w_j \\ + \left( a_6 \right)_j \delta w_{j-1} + \left( a_7 \right)_j \delta g_j + \left( a_8 \right)_j \delta g_{j-1} = \left( r_4 \right)_{j-1/2} \end{aligned} \tag{36}$$

$$\begin{aligned} \left( b_1 \right)_j \delta p_j + \left( b_2 \right)_j \delta p_{j-1} + \left( b_3 \right)_j \delta F_j + \left( b_4 \right)_j \delta F_{j-1} + \left( b_5 \right)_j \delta w_j \\ + \left( b_6 \right)_j \delta w_{j-1} + \left( b_7 \right)_j \delta g_j + \left( b_8 \right)_j \delta g_{j-1} = \left( r_5 \right)_{j-1/2} \end{aligned} \tag{37}$$

where

$$\left( a_1 \right)_j = \left[ \frac{\rho_f}{\rho_{nf}} \frac{1}{\left( 1 - \chi \right)^{2.5}} \left( 1 + \frac{1}{\beta} \right) + h_j \left( \frac{\left( A + \alpha \right)}{2} F_{j-1/2} - \frac{\alpha}{2} F_{j-1/2}^{n-1} \right) \right]$$

$$\left( a_2 \right)_j = \left[ \left( a_1 \right)_j - 2 \frac{\rho_f}{\rho_{nf}} \frac{1}{\left( 1 - \chi \right)^{2.5}} \left( 1 + \frac{1}{\beta} \right) \right]$$

$$\left( a_3 \right)_j = h_j \left[ \frac{\left( A + \alpha \right)}{2} z_{j-1/2} + \frac{\alpha}{2} z_{j-1/2}^{n-1} \right]$$

$$\left( a_4 \right)_j = \left( a_3 \right)_j$$

$$\left( a_5 \right)_j = h_j \left[ -\left( 1 + \alpha \right) w_{j-1/2} - \frac{1}{2} \frac{\rho_f \sigma_{nf}}{\rho_{nf} \sigma_f} M \right]$$

$$\left( a_6 \right)_j = \left( a_5 \right)_j$$

$$\left( a_7 \right)_j = h_j \left[ \frac{\lambda}{2} \left( \frac{\chi \rho_s \left( \beta_s / \beta_f \right) + \left( 1 - \chi \right) \rho_f}{(1 - \chi) \rho_f + \chi \rho_s} \right) \frac{\sin x^{n-1/2}}{x^{n-1/2}} \right]$$

$$\left( a_8 \right)_j = \left( a_7 \right)_j \tag{38}$$

$$\left( b_1 \right)_j = \left[ \frac{1}{\mathrm{Pr}} \frac{k_{nf} / k_f}{\left( (1 - \chi)(\rho \mathrm{C}_p)_f + \chi \left( \rho c_p \right)_s \Big/ \left( \rho c_p \right)_f \right)} + h_j \left( \frac{\left( A + \alpha \right)}{2} F_{j-1/2} - \frac{\alpha}{2} F_{j-1/2}^{n-1} \right) \right]$$

$$\left( b_2 \right)_j = \left[ \frac{2}{\mathrm{Pr}} - \left( b_1 \right)_j \right]$$

$$\left( b_3 \right)_j = h_j \left[ \frac{\left( A + \alpha \right)}{2} p_{j-1/2} + \frac{\alpha}{2} p_{j-1/2}^{n-1} \right]$$

$$\left( b_4 \right)_j = \left( b_3 \right)_j$$

$$\left( b_5 \right)_j = h_j \left[ -\frac{\alpha}{2} g_{j-1/2} + \frac{\alpha}{2} g_{j-1/2}^{n-1} \right] h_j$$

$$
\begin{aligned}
\left(b_6\right)_j &= \left(b_5\right)_j \\
\left(b_7\right)_j &= h_j\left[-\frac{\alpha}{2}w_{j-1/2}-\frac{\alpha}{2}h_j w_{j-1/2}^{n-1}\right] \\
\left(b_8\right)_j &= \left(b_7\right)_j \\
\left(r_1\right)_{j-1/2} &= F_{j-1}-F_j+h_j w_{j-1/2} \\
\left(r_2\right)_{j-1/2} &= w_{j-1}-w_j+h_j z_{j-1/2} \\
\left(r_3\right)_{j-1/2} &= g_{j-1}-g_j+h_j p_{j-1/2} \\
\left(r_4\right)_{j-1/2} &= \frac{\rho_f}{\rho_{nf}}\frac{1}{\left(1-\chi\right)^{2.5}}\left(1+\frac{1}{\beta}\right)\left(z_{j-1}-z_j\right)-\left(A+\alpha\right)h_j F_{j-1/2}z_{j-1/2} \\
&\quad +h_j\left(\alpha z_{j-1/2}F_{j-1/2}^{n-1}-\alpha z_{j-1/2}^{n-1}F_{j-1/2}-\frac{9}{4}\frac{\sin x^{n-1/2}\cos x^{n-1/2}}{x^{n-1/2}}\right) \\
&\quad -h_j\left(\frac{\chi\rho_s\left(\beta_s/\beta_f\right)+\left(1-\chi\right)\rho_f}{(1-\chi)\rho_f+\chi\rho_s}\right)\frac{\lambda}{2}\frac{\sin x^{n-1/2}}{x^{n-1/2}}g_{j-1/2} \\
&\quad +h_j\left(\left(1+\alpha\right)w_{j-1/2}^2+\frac{\rho_f\sigma_{nf}}{\rho_{nf}\sigma_f}Mw_{j-1/2}\right)+\left(R_1\right)_{j-1/2}^{n-1} \\
\left(r_5\right)_{j-1/2} &= \frac{1}{\mathrm{Pr}}\frac{k_{nf}/k_f}{\left((1-\chi)(\rho C_p)_f+\chi\left(\rho c_p\right)_s/\left(\rho c_p\right)_f\right)}\left(p_{j-1}-p_j\right) \\
&\quad -\left(A+\alpha\right)h_j F_{j-1/2}p_{j-1/2}-\alpha h_j p_{j-1/2}^{n-1}F_{j-1/2}+\alpha h_j p_{j-1/2}F_{j-1/2}^{n-1} \\
&\quad +\alpha h_j w_{j-1/2}g_{j-1/2}-\alpha h_j w_{j-1/2}g_{j-1/2}^{n-1}+\alpha h_j w_{j-1/2}^{n-1}g_{j-1/2}+\left(R_2\right)_{j-1/2}^{n-1}
\end{aligned}
\tag{39, 40}
$$

### *3.3. The Block Tridiagonal Matrix*

The matrix form of a linearized tridiagonal system is:

$$\mathrm{A}\delta=\mathrm{r}, \tag{41}$$

where

$$
\mathrm{S}=\begin{bmatrix}
[A_1] & [C_1] & & & & & \\
[B_2] & [A_2] & [C_2] & & & & \\
 & \ddots & \ddots & \ddots & & & \\
 & & & & [B_{J-1}] & [A_{J-1}] & [C_{J-1}] \\
 & & & & & [B_J] & [A_J]
\end{bmatrix},\ \delta=\begin{bmatrix}[\delta_1]\\[\delta_2]\\ \vdots \\ [\delta_{J-1}]\\[\delta_J]\end{bmatrix},\ \mathrm{r}=\begin{bmatrix}[r_1]\\[r_2]\\ \vdots \\ [r_{J-1}]\\[r_J]\end{bmatrix}.
$$

The boundary conditions in Equation (32) are satisfied precisely with no iteration. Due to these suitable values being maintained in every iterate, we assume $\delta F_0=0$, $\delta w_0=0$, $\delta p_0=0$, $\delta w_J=0$, $\delta g_J=0$, and let $d_J=-\frac{1}{2}h_J$.

The entries of the matrices are

$$\left[A_1\right]=\begin{bmatrix} 0 & 0 & 1 & 0 & 0 \\ d_1 & 0 & 0 & d_1 & 0 \\ 0 & -1 & 0 & 0 & d_1 \\ (a_2)_1 & (a_8)_1 & (a_3)_1 & (a_1)_1 & 0 \\ 0 & (b_8)_1 & (b_3)_1 & 0 & (b_1)_1 \end{bmatrix} \tag{42}$$

$$\left[A_j\right]=\begin{bmatrix} d_j & 0 & 0 & 0 & 0 \\ -1 & 0 & 0 & 0 & 0 \\ 0 & -1 & 0 & 0 & 0 \\ (a_6)_j & (a_8)_j & (a_3)_j & (a_1)_j & 0 \\ (b_6)_j & (b_8)_j & (b_3)_j & 0 & (b_1)_j \end{bmatrix},\ 2\le j\le J, \tag{43}$$

$$\left[B_j\right]=\begin{bmatrix} 0 & 0 & -1 & 0 & 0 \\ 0 & 0 & 0 & d_j & 0 \\ 0 & 0 & 0 & 0 & d_j \\ 0 & 0 & (a_4)_j & (a_2)_j & 0 \\ 0 & 0 & (b_4)_j & 0 & (b_2)_j \end{bmatrix},\ 2\le j\le J, \tag{44}$$

$$\left[C_j\right]=\begin{bmatrix} d_j & 0 & 0 & 0 & 0 \\ 1 & 0 & 0 & 0 & 0 \\ 0 & 1 & 0 & 0 & 0 \\ (a_5)_j & (a_7)_j & 0 & 0 & 0 \\ (b_5)_j & (b_7)_j & 0 & 0 & 0 \end{bmatrix},\ 1\le j\le J-1, \tag{45}$$

$$\left[\delta_1\right]=\begin{bmatrix} \delta z_0 \\ \delta g_0 \\ \delta F_1 \\ \delta z_1 \\ \delta p_1 \end{bmatrix},\ \left[\delta_j\right]=\begin{bmatrix} \delta w_{j-1} \\ \delta g_{j-1} \\ \delta F_{j-1} \\ \delta z_{j-1} \\ \delta p_{j-1} \end{bmatrix},\ 2\le j\le J,\ \left[r_j\right]=\begin{bmatrix} (r_1)_{j-(1/2)} \\ (r_2)_{j-(1/2)} \\ (r_3)_{j-(1/2)} \\ (r_4)_{j-(1/2)} \\ (r_5)_{j-(1/2)} \end{bmatrix},\ 1\le j\le J \tag{46}$$

The final step is to solve the system in Equation (41) by the LU (lower–upper) factorization method, then implement numerical operations using MATLAB software (version 7, MathWorks, Natick, MA, USA). In this work the wall shear stress parameter $z(x,0)$ is considered as the convergence criterion (as it is usually considered, see Cebeci and Bradshaw [50]), so the calculations were repeated until the convergence criterion was satisfied, and stopped when $\left|\delta z_0^{(i)}\right|<\varepsilon_1$, where $\varepsilon_1$ is chosen to be $10^{-5}$ which give precise values up to four decimal places.

## 4. Results and Discussion

This section aims to predict and analyze graphically the behavior of a CMC-based Casson nanofluid under the impact of meaningfully related parameters with regard to the velocity, temperature, skin friction coefficient, and local Nusselt number. The ranges of parameters that are taken into consideration are the mixed parameter ( $\lambda>0\&\lambda<0$ ), Casson parameter ( $\beta>0$ ), magnetic parameter ( $M>0$ ) and nanoparticles volume fraction ( $0.1\le\chi\le0.2$ ).

Table 1 shows the thermo-physical properties of CMC-water and the nanoparticles. The numerical results obtained were in a close agreement with the literature and can be seen in comparative Tables 2 and 3.

**Table 1.** Thermo-physical properties of CMC-water (0.0–0.4%) and metals nanoparticles [51].

| Thermo-Physical Property | CMC-Water | Al | Ag | Cu |
|---|---|---|---|---|
| $\rho\left(kg/m^3\right)$ | 997.1 | 2701 | 10,500 | 8933 |
| $C_p\left(J/kgK\right)$ | 4179 | 902 | 235 | 385 |
| $K\left(w/mK\right)$ | 0.613 | 237 | 429 | 401 |
| $\beta\times10^{-5}\left(K^{-1}\right)$ | 21 | 2.31 | 1.89 | 1.67 |
| $\sigma\left(s/m\right)$ | $5.5\times10^{-6}$ | $35\times10^{6}$ | $63\times10^{6}$ | $95.6\times10^{6}$ |
| Pr | 6.2 | - | - | - |

**Table 2.** Comparison of $\mathrm{Re}^{1/2}C_f$ with published findings by Nazar et al. [43] for several values of $\lambda$ $\left(\beta\to\infty, M=0,\ \chi=0, \mathrm{Pr}=0.7\right)$.

| $\lambda$ | −4 | | −1 | | 0 | | 0.74 | | 1 | |
|---|---|---|---|---|---|---|---|---|---|---|
| $x$ | [43] | Present | [43] | Present | [43] | Present | [43] | Present | [43] | Present |
| $0^o$ | 0.0000 | 0.0000 | 0.0000 | 0.0000 | 0.0000 | 0.0000 | 0.0000 | 0.0000 | 0.0000 | 0.0000 |
| $10^o$ | 0.0801 | 0.0780 | 0.3438 | 0.3443 | 0.4160 | 0.4167 | 0.4669 | 0.4545 | 0.4843 | 0.4851 |
| $20^o$ | 0.1149 | 0.1153 | 0.6564 | 0.6500 | 0.8014 | 0.8035 | 0.9031 | 0.8935 | 0.9380 | 0.9279 |
| $30^o$ | | | 0.9098 | 0.9076 | 1.1284 | 1.1244 | 1.2813 | 1.2759 | 1.3335 | 1.3277 |
| $40^o$ | | | 1.0790 | 1.0824 | 1.3733 | 1.3748 | 1.5775 | 1.5778 | 1.6471 | 1.6470 |
| $50^o$ | | | 1.1434 | 1.1537 | 1.5172 | 1.5253 | 1.7737 | 1.7806 | 1.8607 | 1.8672 |
| $60^o$ | | | 1.0866 | 1.1047 | 1.5477 | 1.5630 | 1.8580 | 1.8720 | 1.9627 | 1.9762 |
| $70^o$ | | | 0.8929 | 0.9202 | 1.4583 | 1.4811 | 1.8260 | 1.8470 | 1.9486 | 1.9691 |
| $80^o$ | | | 0.5280 | 0.5680 | 1.2480 | 1.2780 | 1.6800 | 1.7079 | 1.8216 | 1.8489 |
| $90^o$ | | | | | 0.9154 | 0.9530 | 1.4289 | 1.4656 | 1.5915 | 1.6284 |
| $100^o$ | | | | | 0.4308 | 0.4812 | 1.0847 | 1.1351 | 1.2732 | 1.3160 |
| $110^o$ | | | | | | | 0.6543 | 0.7241 | 0.8831 | 0.9559 |
| $120^o$ | | | | | | | | | 0.4220 | 0.5094 |

**Table 3.** Heat transfer coefficient $Q_w(\xi)=-(\partial\theta/\partial\eta)_{\eta=0}$ with published findings by Nazar et al. [43] for several values of $\lambda\left(\beta\to\infty, M=0,\ \chi=0, \mathrm{Pr}=0.7\right)$.

| $\lambda$ | −4 | | −1 | | 0 | | 0.74 | | 1 | |
|---|---|---|---|---|---|---|---|---|---|---|
| $x$ | [43] | Present | [43] | Present | [43] | Present | [43] | Present | [43] | Present |
| $0^o$ | 0.6534 | 0.6519 | 0.7870 | 0.7858 | 0.8162 | 0.8150 | 0.8354 | 0.8342 | 0.8463 | 0.8406 |
| $10^o$ | 0.6440 | 0.6435 | 0.7818 | 0.7812 | 0.8112 | 0.8104 | 0.8307 | 0.8301 | 0.8371 | 0.8362 |
| $20^o$ | 0.6150 | 0.6158 | 0.7669 | 0.7670 | 0.7974 | 0.7974 | 0.8173 | 0.8174 | 0.8239 | 0.8239 |
| $30^o$ | | | 0.7422 | 0.7433 | 0.7746 | 0.7747 | 0.7955 | 0.7963 | 0.8024 | 0.8031 |
| $40^o$ | | | 0.7076 | 0.7097 | 0.7429 | 0.7447 | 0.7652 | 0.7669 | 0.7725 | 0.7741 |
| $50^o$ | | | 0.6624 | 0.6658 | 0.7022 | 0.7039 | 0.7267 | 0.7293 | 0.7345 | 0.7371 |
| $60^o$ | | | 0.6055 | 0.6103 | 0.6525 | 0.6565 | 0.6800 | 0.6837 | 0.6887 | 0.6922 |
| $70^o$ | | | 0.5224 | 0.5403 | 0.5934 | 0.5986 | 0.6253 | 0.6300 | 0.6352 | 0.6397 |
| $80^o$ | | | 0.4342 | 0.4432 | 0.5236 | 0.5287 | 0.5672 | 0.5671 | 0.5742 | 0.5784 |
| $90^o$ | | | | | 0.4398 | 0.4382 | 0.4920 | 0.4887 | 0.5060 | 0.5025 |
| $100^o$ | | | | | 0.3263 | 0.3197 | 0.4120 | 0.3978 | 0.4304 | 0.4152 |
| $110^o$ | | | | | | | 0.3179 | 0.3004 | 0.3458 | 0.3246 |
| $120^o$ | | | | | | | | | 0.2442 | 0.2314 |

Figures 2 and 3 display the influence of the mixed parameter in opposing and assisting flow cases ($\lambda > 0 \& \lambda < 0$) on the skin friction coefficient and Nusselt number, respectively. From these figures, we found that the Al–CMC-water has the highest skin friction coefficient values in the case of assisting flow and the lowest in the case of the opposing flow. For the Nusselt number, Al–CMC-water has the highest value in both cases ($\lambda > 0 \& \lambda < 0$) and this is due to the thermo-physical properties that the aluminum possesses. It can also be observed that, in both the cases of opposing and assisting flow, when $\lambda$ increases, $\mathrm{Re}^{1/2} C_f$ and $\mathrm{Re}^{-1/2} Nu$ increase due to increase in the buoyancy force.

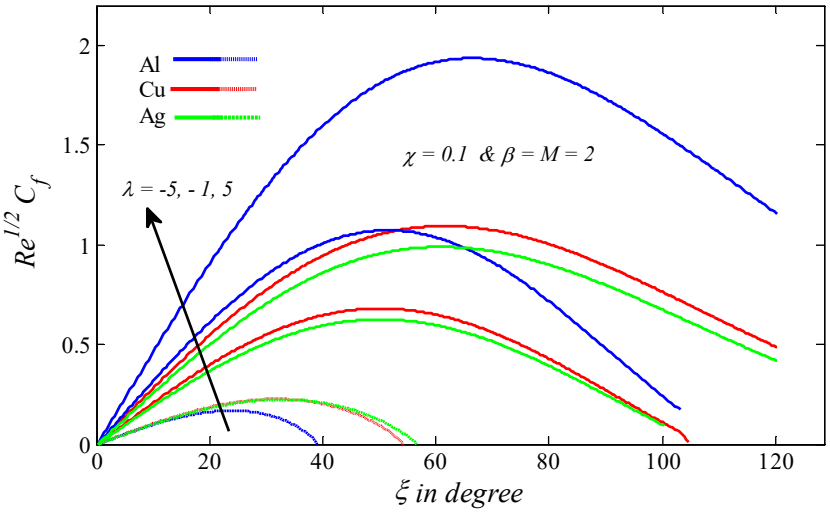


**Figure 2.** Mixed parameter versus the local skin friction.

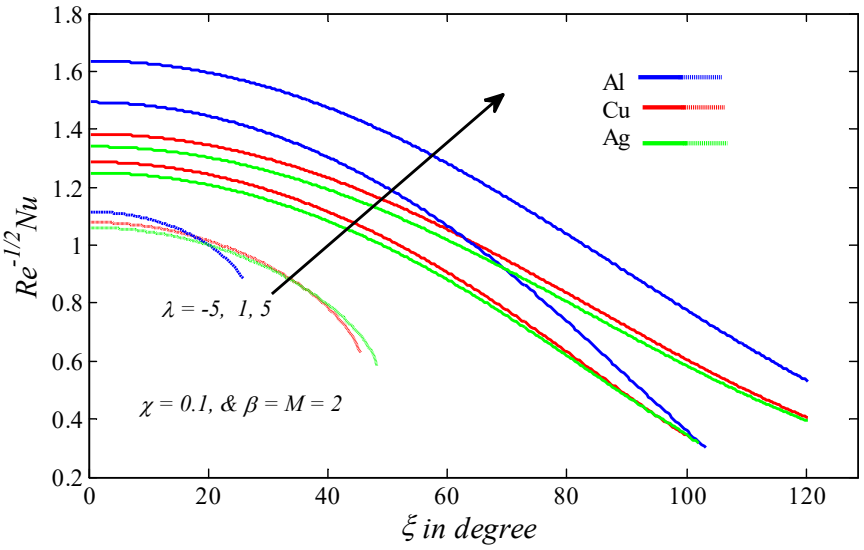


**Figure 3.** Mixed parameter versus the local Nusselt number.

In Figures 4 and 5 it can be seen that the increment in the value of nanoparticles volume fraction $\chi$ resulted in a noteworthy improvement in both the skin friction coefficient and Nusselt number. The improvement in the Nusselt number is caused by the enhancement of the density and thermal conductivity of CMC-water.

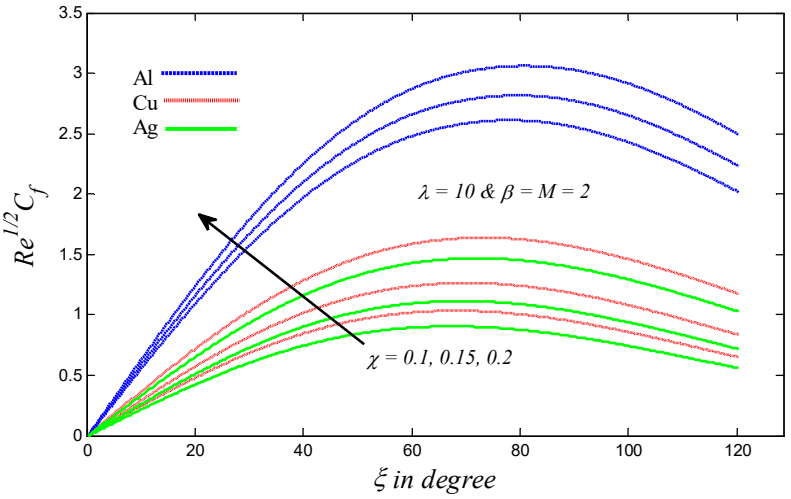


**Figure 4.** Nanoparticles volume fraction versus the local skin friction coefficient.

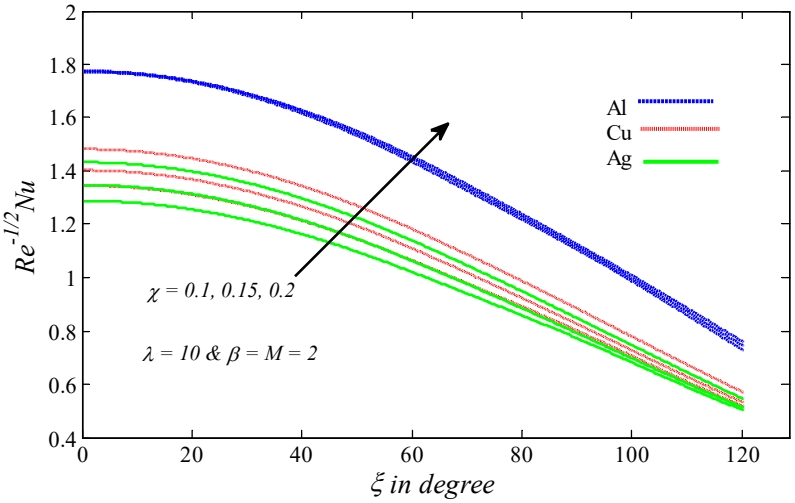


**Figure 5.** Nanoparticles volume fraction versus the local Nusselt number.

Figures 6 and 7 show the relationship between $\beta$ and both the skin friction coefficient, and Nusselt number respectively. It's noticed that the Casson parameter $\beta$ is inversely proportional to the skin friction coefficient, but it is directly proportional to the Nusselt number. Physically, when the values of $\beta$ rise, the yield stress decreases and therefore the skin friction coefficient decreases.

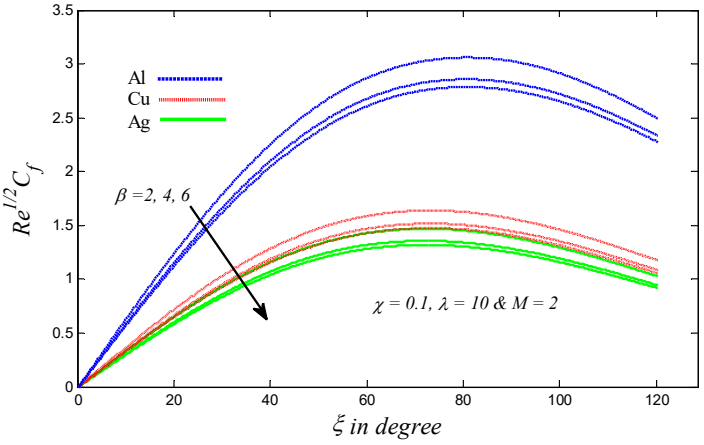


**Figure 6.** Casson parameter versus the local skin friction coefficient.

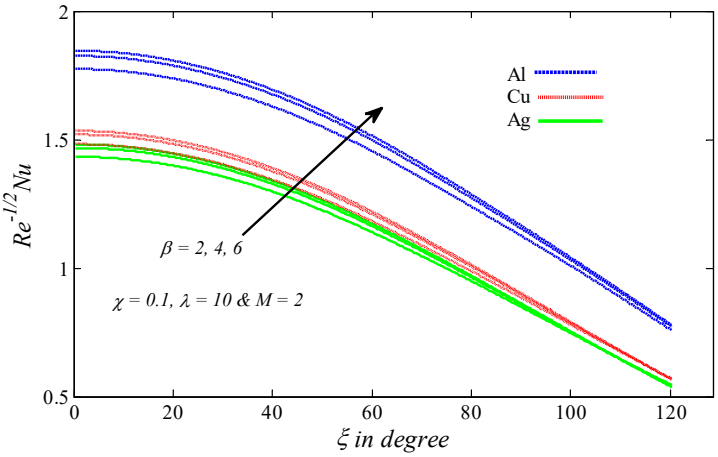


**Figure 7.** Casson parameter versus the local Nusselt number.

Figures 8 and 9 illustrate the graphical findings of $\mathrm{Re}^{1/2} C_f$ and $\mathrm{Re}^{-1/2} Nu$ respectively, with various values of the magnetic parameter ( $M$ ). It is clear that as the values of $M$ grow, both the skin friction coefficient and Nusselt number decline. In fact, this decline is a result of the restraining that occurred in the fluid flow, caused by the increase in intensity of the magnetic current which curbs convection and thereby reduces the skin fraction coefficient and Nusselt number. Furthermore, these figures demonstrate that, whatever the values of parameters $\lambda, \chi, \beta$ or $M$, Al–CMC-water has the highest $\mathrm{Re}^{1/2} C_f$ and $\mathrm{Re}^{-1/2} Nu$.

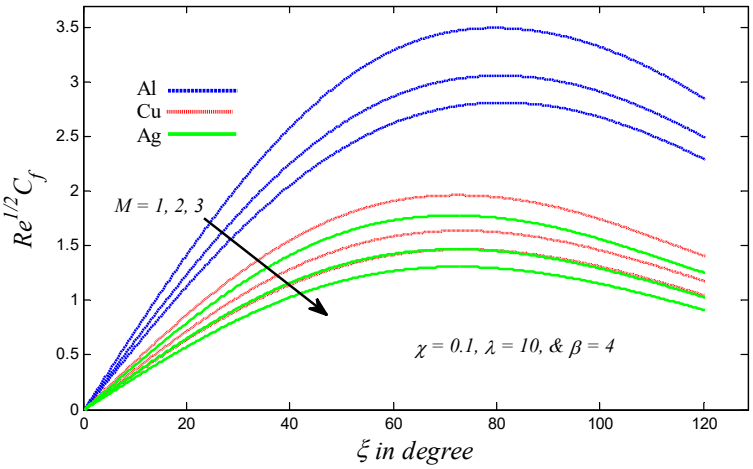


**Figure 8.** Magnetic parameter versus the local skin friction coefficient.

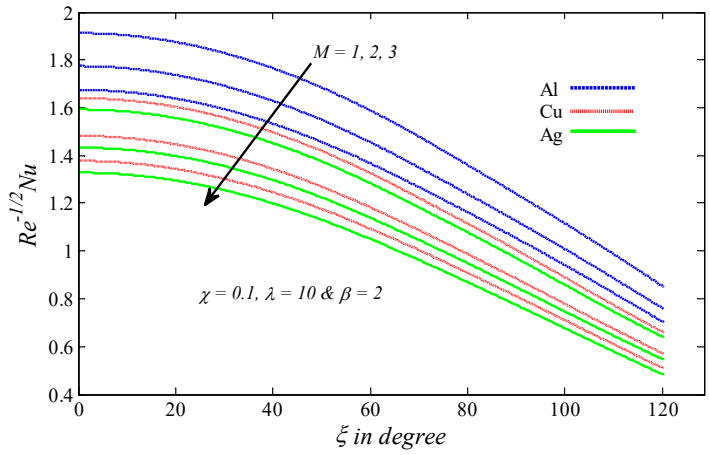

**Figure 9.** Magnetic parameter versus the local Nusselt number.

Figures 10 and 11 demonstrate the impact of the mixed parameter $\lambda$ on the velocity and temperature in both cases opposing and assisting flow ($\lambda > 0 \& \lambda < 0$). Both the cases of flow indicate that an increment in $\lambda$ is accompanied by an improvement in the velocity or a decay in the temperature profiles. In fact, the growth in the mixed parameter enhances the thermal buoyancy force—and, hence the velocity increases.

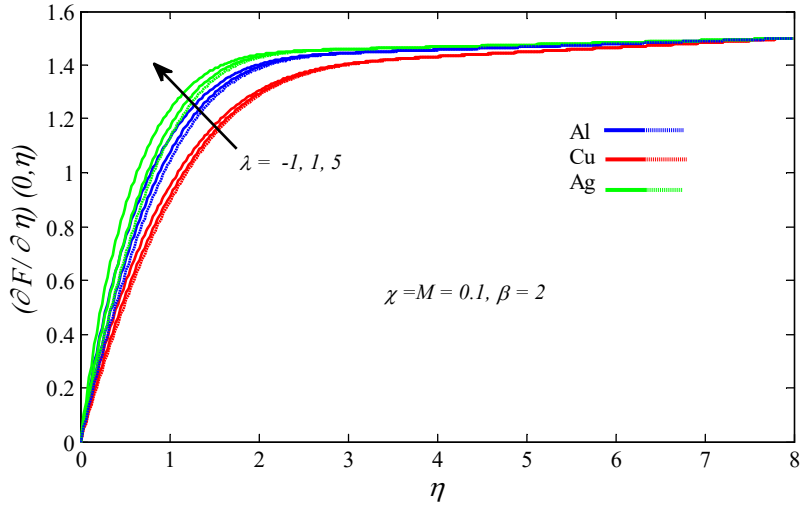


**Figure 10.** Mixed parameter versus velocity.

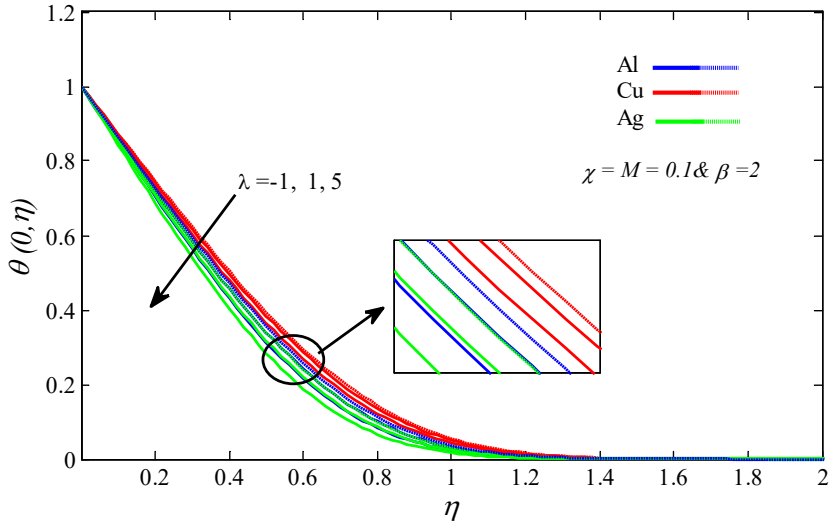


**Figure 11.** Mixed parameter versus temperature.

Figures 12 and 13 confirmed that the effect of the nanoparticles volume fraction ($\chi$), on both velocity and temperature, is a positive effect. A rise in $\chi$ leads to a quicker transfer of heat from the outside of the sphere to the fluid and thus aids in the augmentation of the thickness of the thermal layer due to the increase in the temperature of the fluid. In addition, the increase in $\chi$ enhances energy transmission, which increases the fluid velocity. According to Figures 14 and 15, higher values of the Casson parameter ($\beta$) cause a curb in the velocity and temperature, which is verifiable because the augmentation in $\beta$ creates a resistance force that restricts the flow of the fluid, which restrains the nanofluid velocity.

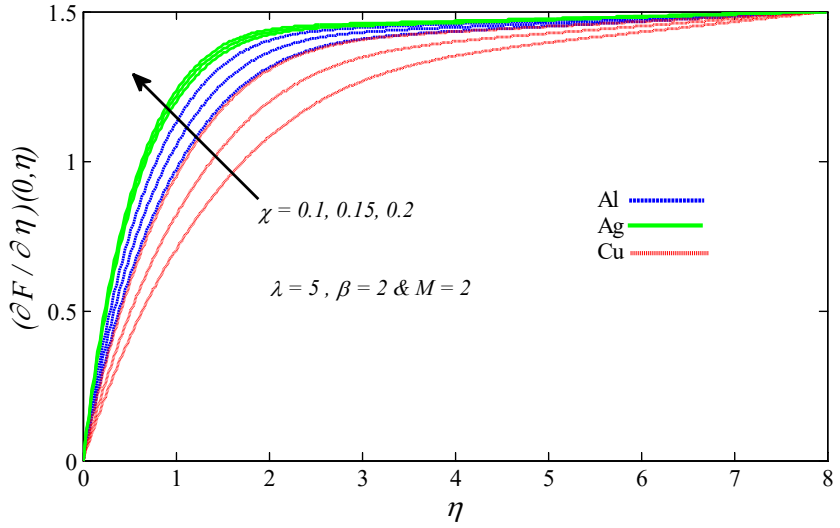


**Figure 12.** Nanoparticles volume fraction versus velocity.

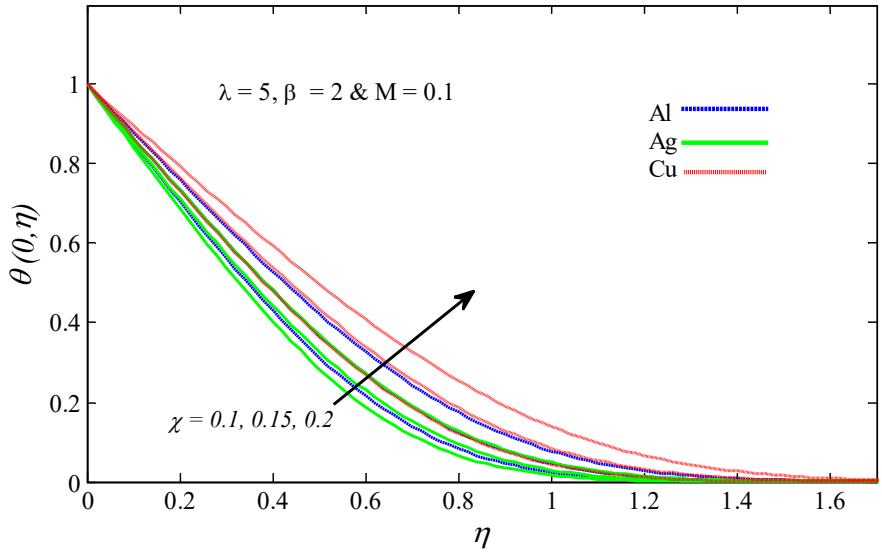


**Figure 13.** Nanoparticles volume fraction versus temperature.

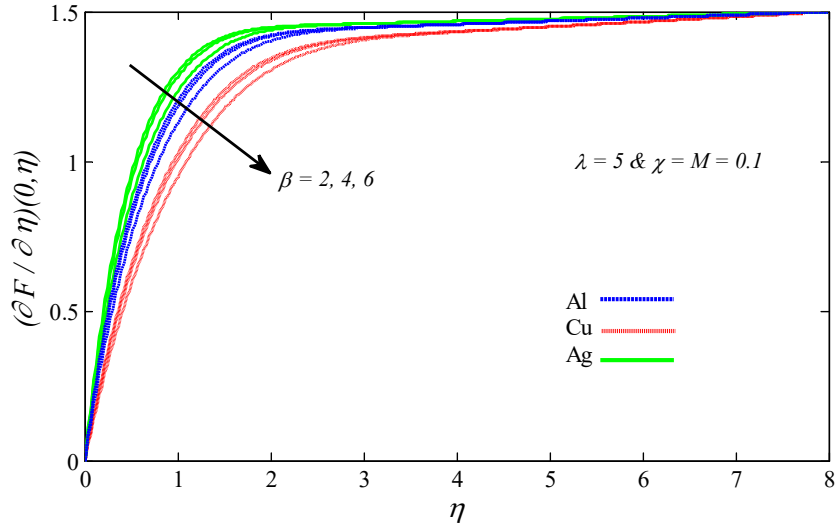


**Figure 14.** Casson parameter versus velocity.

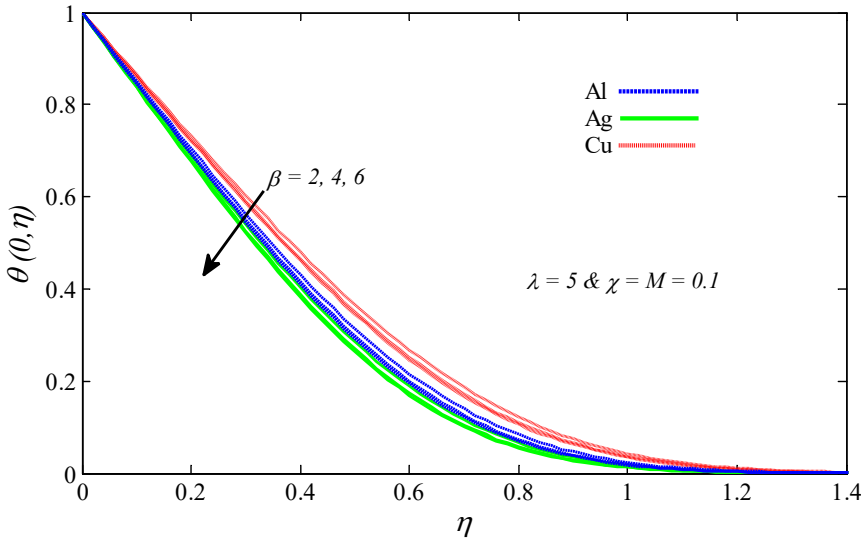


**Figure 15.** Casson parameter versus temperature.

Figures 16 and 17 depict the graphical findings of temperature and velocity versus the magnetic parameter ( $M$ ), respectively. It is evident in these figures that as the value of $M$ grows, the temperature increases but the velocity decreases. This phenomenon occurs when a magnetic current passes through a flowing nanofluid, which produces a kind of force known as the Lorentz force and, consequently, resists the nanofluid movement. It is worth noting that, whatever the values of parameters $\lambda, \chi, \beta$ or $M$, Silver–CMC-water is superior in terms of velocity, and we found that the Copper–CMC-water temperature was the highest.

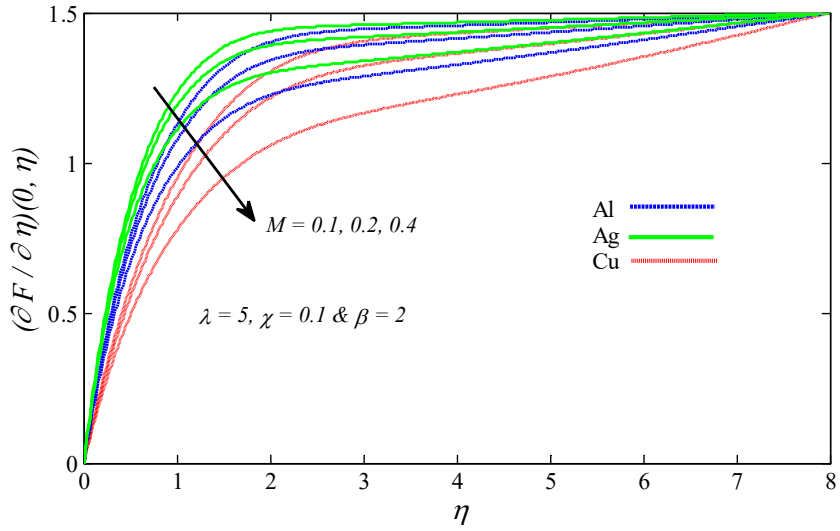


**Figure 16.** Magnetic parameter versus velocity.

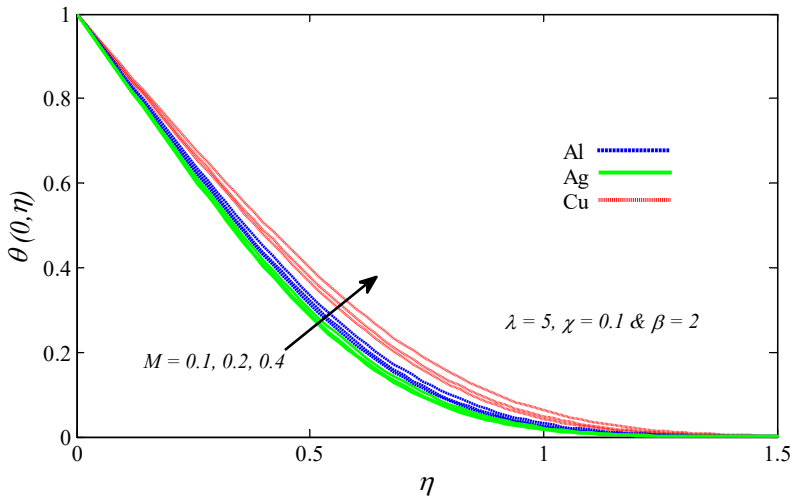


**Figure 17.** Magnetic parameter versus temperature.

## 5. Conclusions

In this research, we have explored the behavior of a CMC-water based Casson nanofluid from a solid sphere produced by mixed convection under a MHD influence. The following meaningful observations are worth mentioning:

1. The temperature profile increases when the values of each of $\chi$ or $M$ parameters grow, and decreases as the values of $\beta$ or $\lambda$ increase.
2. The nanoparticles volume fraction has a positive relationship with all the physical quantities examined in this research.
3. The skin friction, velocity, and Nusselt number are decreasing functions of the magnetic field intensity, whereas temperature is an increasing function of it.

Regardless of the values of examined parameters, the values of temperature for Cu–CMC-water were the highest and had the lowest velocity.

**Author Contributions:** F.A.A.: Formal analysis, Investigation, and Methodology; F.A.A. and H.T.A.: Software; R.I. H.T.A. and A.M.R.: Supervision; H.T.A., A.M.R. and R.I.: Validation; H.T.A., A.M.R. and R.I.: Writing–review & editing. All authors have read and agreed to the published version of the manuscript.

**Funding:** This research was funded by University Malaysia Terengganu (UMT) through grant vote number 55193/4.

**Conflicts of Interest:** The authors declare no conflict of interest.

## Nomenclature

| | | | |
|---|---|---|---|
| $a$ | Radius of Cylinder | $\alpha$ | Thermal diffusivity |
| $B_0$ | Magnetic field strength | $\beta$ | Casson parameter |
| $C_f$ . | Skin friction coefficient | $\beta_f$ | Thermal expansion of base fluid |
| $r(\xi)$ | Radial Distance | $\beta_s$ | Thermal expansion of nanoparticles |
| $Gr$ | Grashof number | $\theta$ | Temperature of nanofluid |
| g | Gravity vector | $\mu_\beta$ | Plastic Dynamic viscosity of base fluid |

| | | | |
|---|---|---|---|
| $k$ . | Thermal conductivity | $\mu_f$ | Dynamic viscosity of base fluid |
| $M$ | Magnetic parameter | $\rho$ | Density |
| $Nu$ | Nusselt Number | $\left(\rho c_p\right)$ | Heat capacity |
| Pr | Prandtl number | $\tau_w$ | Wall shear stress |
| $p_y$ | Yield stress | $\chi$ | Nanoparticle volume fraction |
| $T$ | Temperature of the fluid | $\psi$ | Stream function |
| $T_w$ | Wall temperature | $\sigma$ | Electrical conductivity |
| $T_\infty$ | Ambient temperature | $\lambda$ | Mixed parameter |
| $u$ | $\xi$ - component of velocity | Subscript | |
| $v$ . | $\eta$ - component of velocity | $s$ | nanoparticles |
| $v_f$ | Kinematic viscosity | $nf$ | Nanofluid |
| $u_e$ | Free stream velocity | $f$ | Base fluid |

## References


1. Mondal, I.H. *Carboxymethyl Cellulose: Synthesis and Characterization*; Nova Science Publishers: Hauppauge, NY, USA, 2019.
2. Benchabane, A.; Bekkour, K. Rheological properties of carboxymethyl cellulose (CMC) solutions. *Colloid Polym. Sci.* **2008**, *286*, 1173.
3. Bekkour, K.; Sun-Waterhouse, D.; Wadhwa, S.S. Rheological properties and cloud point of aqueous carboxymethyl cellulose dispersions as modified by high or low methoxyl pectin. *Food Res. Int.* **2014**, *66*, 247–256.
4. Babazadeh, A.; Tabibiazar, M.; Hamishehkar, H.; Shi, B. Zein-CMC-PEG multiple nanocolloidal systems as a novel approach for nutra-pharmaceutical applications. *Adv. Pharm. Bull.* **2019**, *9*, 262.
5. Karabinos, J.; Hindert, M. Carboxymethylcellulose. In *Advances in Carbohydrate Chemistry*; Elsevier: Amsterdam, The Netherlands, 1954; pp. 285–302.
6. Hollabaugh, C.; Burt, L.H.; Walsh, A.P. Carboxymethylcellulose. Uses and applications. *Ind. Eng. Chem.* **1945**, *37*, 943–947.
7. Mondal, I.H. *Carboxymethyl Cellulose: Pharmaceutical and Industrial Applications*; Nova Science Publishers: Hauppauge, NY, USA, 2019.
8. Grządka, E.; Matusiak, J.; Bastrzyk, A.; Polowczyk, I. CMC as a stabiliser of metal oxide suspensions. *Cellulose* **2020**, *27*, 2225–2236.
9. Chen, J.; Li, H.; Fang, C.; Cheng, Y.; Tan, T.; Han, H. Synthesis and structure of carboxymethylcellulose with a high degree of substitution derived from waste disposable paper cups. *Carbohydr. Polym.* **2020**, *2020*, 116040.
10. Novak, U.; Bajić, M.; Kõrge, K.; Oberlintner, A.; Murn, J.; Lokar, K.; Triler, K.V.; Likozar, B. From waste/residual marine biomass to active biopolymer-based packaging film materials for food industry applications–a review. *Phys. Sci. Rev.* **2019**, *5*, e0099.
11. Saqib, M.; Khan, I.; Shafie, S. Natural convection channel flow of CMC-based CNTs nanofluid. *Eur. Phys. J. Plus* **2018**, *133*, 549.
12. Saqib, M.; Khan, I.; Shafie, S. Application of Atangana–Baleanu fractional derivative to MHD channel flow of CMC-based-CNT's nanofluid through a porous medium. *Chaos Soliton. Fract.* **2018**, *116*, 79–85.

13. Rahmati, A.R.; Akbari, O.A.; Marzban, A.; Toghraie, D.; Karimi, R.; Pourfattah, F. Simultaneous investigations the effects of non-Newtonian nanofluid flow in different volume fractions of solid nanoparticles with slip and no-slip boundary conditions. *Sci. Eng. Por.* **2018**, *5*, 263–277.
14. Feynman, R.P. There's plenty of room at the bottom. California Institute of Technology. In *Engineering and Science Magazine*; California Institute of Technology: Pasadena, CA, USA, 1960.
15. Choi, S.U.; Eastman, J.A. *Enhancing Thermal Conductivity of Fluids with Nanoparticles*; Argonne National Lab.: Lemont, IL, USA, 1995.
16. Buongiorno, J. Convective transport in nanofluids. *J. Heat Transf.* **2006**, *128*, 240–250.
17. Tiwari, R.K.; Das, M.K. Heat transfer augmentation in a two-sided lid-driven differentially heated square cavity utilizing nanofluids. *Int. J. Heat Mass Tran.* **2007**, *50*, 2002–2018.
18. Swalmeh, M.Z.; Alkasasbeh, H.T.; Hussanan, A.; Mamat, M. Heat transfer flow of Cu-water and Al2O3-water micropolar nanofluids about a solid sphere in the presence of natural convection using Keller-box method. *Res. Phys.* **2018**, *9*, 717–724.
19. Selimefendigil, F.; Chamkha, A.J. Magnetohydrodynamics mixed convection in a power law nanofluid-filled triangular cavity with an opening using Tiwari and Das' nanofluid model. *J. Anal. Calorim.* **2019**, *135*, 419–436.
20. Alwawi, F.A.; Alkasasbeh, H.T.; Rashad, A.; Idris, R. MHD natural convection of Sodium Alginate Casson nanofluid over a solid sphere. *Res. Phys.* **2020**, *16*, 102818.
21. Mathur, P.; Jha, S.; Ramteke, S.; Jain, N. Pharmaceutical aspects of silver nanoparticles. *Artif. CellsNanomed. Biotechnol.* **2018**, *46*, 115–126.
22. Bonde, H.C.; Fojan, P.; Popok, V.N. Controllable embedding of size-selected copper nanoparticles into polymer films. *Plasma Process Polym.* **2020**, *17*, 1900237.
23. dos Santos, C.A.; Ingle, A.P.; Rai, M. The emerging role of metallic nanoparticles in food. *Appl. Microbiol. Biotechnol.* **2020**, *104*, 2373–2383.
24. Makinde, O.; Aziz, A. MHD mixed convection from a vertical plate embedded in a porous medium with a convective boundary condition. *Int. J. Sci.* **2010**, *49*, 1813–1820.
25. Tham, L.; Nazar, R.; Pop, I. Mixed convection boundary-layer flow about an isothermal solid sphere in a nanofluid. *Phys. Scr.* **2011**, *84*, 025403.
26. Chamkha, A.J.; Rashad, A.; Alsabery, A.; Abdelrahman, Z.; Nabwey, H.A. Impact of Partial Slip on Magneto-Ferrofluids Mixed Convection Flow in Enclosure. *J. Sci. Eng. Appl.* **2020**, 1–25.
27. Waqas, M.; Farooq, M.; Khan, M.I.; Alsaedi, A.; Hayat, T.; Yasmeen, T. Magnetohydrodynamic (MHD) mixed convection flow of micropolar liquid due to nonlinear stretched sheet with convective condition. *Int. J. Heat Mass Tran.* **2016**, *102*, 766–772.
28. Makinde, O.; Mabood, F.; Khan, W.; Tshehla, M. MHD flow of a variable viscosity nanofluid over a radially stretching convective surface with radiative heat. *J. Mol. Liq.* **2016**, *219*, 624–630.
29. Chamkha, A.; Rashad, A.; Mansour, M.; Armaghani, T.; Ghalambaz, M. Effects of heat sink and source and entropy generation on MHD mixed convection of a Cu-water nanofluid in a lid-driven square porous enclosure with partial slip. *Phys. Fluids* **2017**, *29*, 052001.
30. Rashad, A.; Mansour, M.; Armaghani, T.; Chamkha, A. MHD mixed convection and entropy generation of nanofluid in a lid-driven U-shaped cavity with internal heat and partial slip. *Phys. Fluids* **2019**, *31*, 042006.
31. Alkasasbeh, H.T.; Swalmeh, M.Z.; Hussanan, A.; Mamat, M. Effects of mixed convection on methanol and kerosene oil based micropolar nanofluid containing oxide nanoparticles. *CFD Lett.* **2019**, *11*, 55–68.
32. Swalmeh, M.Z.; Alkasasbeh, H.T.; Hussanan, A.; Mamat, M. Numerical investigation of heat transfer enhancement with Ag-GO water and kerosene oil based micropolar nanofluid over a solid sphere. *Adva. Res. Fluid. Mech. Sci.* **2019**, *59*, 269–282.
33. Casson, N. A flow equation for pigment-oil suspensions of the printing ink type. *Rheol. Disperse Syst.* **1959**, *2*, 84–102.
34. Malik, M.; Naseer, M.; Nadeem, S.; Rehman, A. The boundary layer flow of Casson nanofluid over a vertical exponentially stretching cylinder. *Appl. Nanosci.* **2014**, *4*, 869–873.
35. Mukhopadhyay, S.; Mondal, I.C.; Chamkha, A.J. Casson fluid flow and heat transfer past a symmetric wedge. *Heat. Transf. Asian. Res.* **2013**, *42*, 665–675.
36. Mustafa, M.; Hayat, T.; Ioan, P.; Hendi, A. Stagnation-point flow and heat transfer of a Casson fluid towards a stretching sheet. *Z. Nat. A* **2012**, *67*, 70–76.

37. Ghadikolaei, S.; Hosseinzadeh, K.; Ganji, D.; Jafari, B. Nonlinear thermal radiation effect on magneto Casson nanofluid flow with Joule heating effect over an inclined porous stretching sheet. *Case Stud. Eng.* **2018**, *12*, 176–187.
38. Rafique, K.; Anwar, M.I.; Misiran, M.; Khan, I.; Alharbi, S.; Thounthong, P.; Nisar, K. Numerical Solution of Casson Nanofluid Flow Over a Non-linear Inclined Surface With Soret and Dufour Effects by Keller-Box Method. *Front. Phys.* **2019**, *7*, 00139
39. Alwawi, F.A.; Alkasasbeh, H.T.; Rashad, A.M.; Idris, R. Natural convection flow of Sodium Alginate based Casson nanofluid about a solid sphere in the presence of a magnetic field with constant surface heat flux. *J. Phys. Conf. Ser.* **2019**, *1366*, 012005.
40. Alwawi, F.A.; Alkasasbeh, H.T.; Rashad, A.; Idris, R. Heat transfer analysis of ethylene glycol-based Casson nanofluid around a horizontal circular cylinder with MHD effect. *Proc. Inst. Mech. Eng. Part C J. Mech. Eng. Sci.* **2020**, 0954406220908624.
41. Alkasasbeh, H.; Swalmeh, M.; Bani Saeed, H.; Al Faqih, F.; Talafha, A. Investigation on CNTs-Water and Human Blood based Casson Nanofluid Flow over a Stretching Sheet under Impact of Magnetic Field. *Front. Heat Mass Transf.* **2020**, *14*, 15.
42. Huang, M.; Chen, G. Laminar free convection from a sphere with blowing and suction. *J. Heat Transf.* **1987**, *109*, 6068496.
43. Nazar, R.; Amin, N.; Pop, I. Mixed convection boundary layer flow about an isothermal sphere in a micropolar fluid. *Int. J. Sci.* **2003**, *42*, 283–293.
44. Molla, M.M.; Rahman, A.; Rahman, L.T. Natural convection flow from an isothermal sphere with temperature dependent thermal conductivity. *J. Nav. Archit. Mar. Eng.* **2005**, *2*, 53–64.
45. Ahmed, S.E.; Mansour, M.; Hussein, A.K.; Mallikarjuna, B.; Almeshaal, M.A.; Kolsi, L. MHD mixed convection in an inclined cavity containing adiabatic obstacle and filled with Cu–water nanofluid in the presence of the heat generation and partial slip. *J. Anal. Calorim.* **2019**, *138*, 1443–1460.
46. Rashad, A.; Chamkha, A.J.; El-Kabeir, S. Effect of chemical reaction on heat and mass transfer by mixed convection flow about a sphere in a saturated porous media. *Int. J. Numer. Method H* **2011**, *21*, 418–433.
47. Molla, M.M.; Hossain, M.; Taher, M. Magnetohydrodynamic natural convection flow on a sphere with uniform heat flux in presence of heat generation. *Acta Mech.* **2006**, *186*, 75.
48. Keller, H.; Bramble, J. Numerical solutions of partial differential equations. *Mathematics* **1970**, *1*, 81–94.
49. Jones, E. An asymptotic outer solution applied to the Keller box method. *J. Comput. Phys.* **1981**, *40*, 411–429.
50. Cebeci, T.; Bradshaw, P. *Physical and Computational Aspects of Convective Heat Transfer*; Springer Science & Business Media, New York, NY, USA, 2012; p. 487.
51. Das, S.; Banu, A.; Jana, R.; Makinde, O. Entropy analysis on MHD pseudo-plastic nanofluid flow through a vertical porous channel with convective heating. *AEJ* **2015**, *54*, 325–337.


© 2020 by the authors. Licensee MDPI, Basel, Switzerland. This article is an open access article distributed under the terms and conditions of the Creative Commons Attribution (CC BY) license (http://creativecommons.org/licenses/by/4.0/).